JOURNAL OF GEOPHYSICAL RESEARCH, VOL. 102, NO. C8, PAGES 18,723–18,736, AUGUST 15, 1997

Correlation of oceanographic signatures appearing in synthetic aperture radar and interferometric synthetic aperture radar imagery with in situ measurements

G. O. Marmorino,[1] D. R. Thompson,[2] H. C. Graber,[3] and C. L. Trump[1]

Abstract. Synthetic aperture radar (SAR) imagery collected over the continental shelf near Cape Hatteras, N. C., is analyzed in conjunction with shipboard hydrographic and current measurements. The SAR measurements were made over a 2-hour period on June 20, 1993, in both standard mapping mode and interferometric synthetic aperture radar (INSAR) mode from a NASA DC-8 aircraft as part of the High-Resolution Remote Sensing Experiment. In situ currents were measured using a surface-towed acoustic Doppler current profiler (ADCP). The measurements were made near the end of a period of Gulf Stream incursion onto the shelf as detected using a shore-based HF radar. Winds were southwesterly at 4–6 m s^{-1}. Long, curvilinear SAR signatures, resembling earlier SEASAT observations made in the same area, are shown to correspond to narrow, shallow fronts separating water masses that increase in surface density with distance offshore. Across-front changes in surface current inferred from the INSAR data are consistent with 2-m-depth currents measured by the ADCP over scales of tens of meters. Thus frontal current gradients measured by INSAR reflect real changes in surface current and are not due to biases induced by changes in the surface-wave spectrum. This lends support to the detailed INSAR surface maps derived by *Graber et al.* [1996]. An east-west salinity front having the largest observed surface density and current gradient is corrugated on length scales up to the local Rossby radius of deformation and translates southward between successive images. In data from the longer radar wavelengths the salinity front appears as a dark band downwind of a bright signature, and this is interpreted as a region where Bragg-scale waves regenerate following their dissipation in the frontal region. In addition to the fronts the imagery shows closely spaced packets of southward propagating ocean internal waves occurring in the strongly stratified inshore water mass. This case study further serves to emphasize the potential of SAR imagery for study of a wide range of shelf processes.

1. Introduction

Since the launch of SEASAT in 1978, there has been great interest in synthetic aperture radar (SAR) imaging of oceanographic features [*Fu and Holt*, 1982; *Gasparovic et al.*, 1988; *Phillips*, 1988; *Marmorino et al.*, 1994; *Nilsson and Tildesley*, 1995; *Johannessen et al.*, 1993, 1996; *Beal et al.*, 1997]. These papers give examples of SAR imagery showing oceanographic features such as fronts and internal waves that are typically imaged in coastal areas under moderate winds. Qualitatively, variations in surface current associated with these features can modulate the oceanic surface-wave spectrum. This modulation produces a differential surface roughening that causes a corresponding change in the intensity of the backscattered radar signal that renders the features visible in the imagery. In general, the intensity of the radar modulation depends not only on the strength of the current gradient but also on the local wind velocity as well as the radar frequency and imaging geometry. When the roughness height of the ocean surface is smaller than the radar wavelength, the modulation of the backscattered signal is sensitive to changes in the so-called Bragg component of the surface-wave spectrum. For microwave radars the length scales of these Bragg components range from about a meter to a few millimeters. Furthermore, it is generally true that for a fixed current gradient, longer components of the wave spectrum receive a larger modulation. This is because the shorter waves respond more quickly to the local wind and are rapidly regenerated when perturbed by variable currents. Significant modulation patterns can, however, appear in SAR imagery even when there is little or no direct modulation of the Bragg spectral components. This is because spectral modulations at longer wavelengths can result, for example, in variations in the local incidence angle (so-called tilt modulation) that can also affect the backscattered signal. For a more quantitative discussion of this wave-current interaction process and its effect on radar backscatter see for example, *Thompson et al.* [1988] as well as other papers appearing in Georgia Strait and SAR Internal Wave Signature Experiments special section, *Journal of Geophysical Research*, *93*(C10), 12,217–12,536, 1988. In general, for a SAR image collected at the lower microwave frequencies such as L band (1 GHz) we can expect regions with surface-current convergence (negative horizontal surface-current gradient) to appear as relatively bright signatures, with

[1]Naval Research Laboratory, Washington, D. C.
[2]Applied Physics Laboratory, Johns Hopkins University, Laurel, Maryland.
[3]Rosenstiel School of Marine and Atmospheric Science, University of Miami, Miami, Florida.

Paper number 97JC01450.
0148-0227/97/97JC-01450$09.00

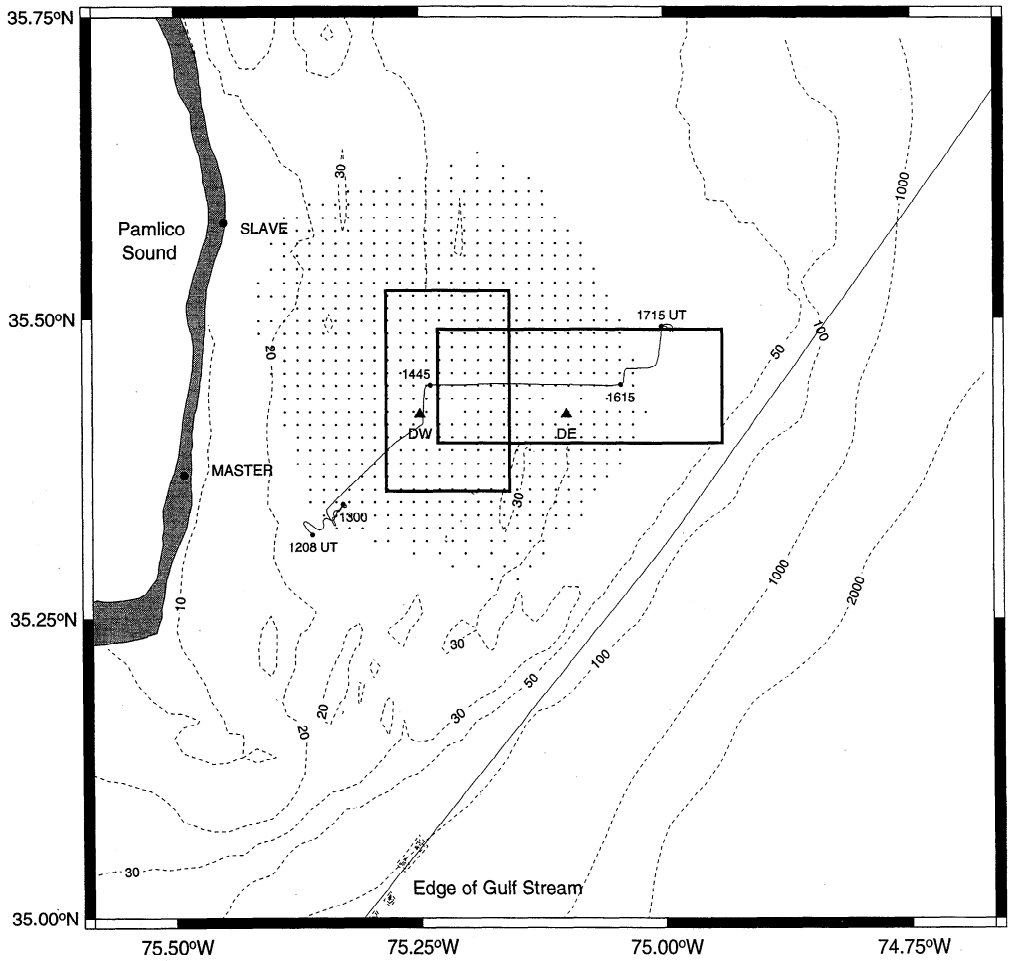

Figure 1. Study area showing location of synthetic aperture radar (SAR) images (rectangles), track of USNS *Bartlett* (1208–1715 UT), ocean surface current radar (OSCR) shore stations and measurement cells (dots), and DW and DE moorings (triangles). Diagonal line near the shelf break shows the mean position of the inshore edge of Gulf Stream surface water.

divergence (positive gradient) to appear as relatively dark, with internal waves to appear as bright-dark pairs, and with fronts with both convergence and shear to appear as either bright or dark depending on the relative orientation of the front and radar illumination and the relative strength of the frontal shear and convergence [*Johannessen et al.*, 1996].

On the basis of an understanding of these and other effects a goal of ocean remote sensing is to use SAR imagery to extract quantitative geophysical information, such as current gradients and water column stratification [e.g., *Johannessen et al.*, 1996; *Porter and Thompson*, 1996]. Progress toward this goal has been limited by an insufficient number of studies having in situ oceanic and atmospheric measurements taken simultaneously with the radar observations. To advance our understanding, field measurements were conducted in September 1991 and June 1993 as part of the High-Resolution Remote Sensing Program [*Herr et al.*, 1991]. The area chosen for study was the continental shelf region northeast of Cape Hatteras (Figure 1). This is an area rich in frontogenic interactions between coastal water masses and water derived from the Gulf Stream [e.g., *Gawarkiewicz et al.*, 1992; *Marmorino and Trump*, 1994; *Mied et al.*, 1996]. Intrusions of high-speed northeastward flow recur over the shelf at 3–5 day intervals [*Chemi et al.*, 1993; *Shay et al.*, 1995], which is comparable to the long-term recurrence interval of 4–5 days for Gulf Stream frontal eddies in the vicinity of Cape Hatteras [*Glenn and Ebbesmeyer*, 1994]. As the hydrography over the shelf is often dominated by salinity changes, imaging radars should be of value in detecting water mass boundaries or tracking these boundaries in concert with satellite infrared imagery [e.g., *Johannessen et al.*, 1996]. Examples of early SAR imagery collected over the study area are shown by *Hayes* [1981] and *Fu and Holt* [1982; images 13 and 26]. These show numerous bright, 10-km-long filaments lying northeast of Cape Hatteras and inshore of the Gulf Stream. Fu and Holt conjectured that such SAR signatures lying over the shelf are manifestations of an interaction between Gulf Stream and shelf waters, but no in situ data existed to explore this.

In this paper a case study is made of spatially overlapping airborne SAR images collected on June 20, 1993 (Figure 1). These data were obtained in conjunction with shipboard hydrographic and current measurements, supplementary data being available from a shore-based HF radar and two moorings. The SAR and HF measurements are also analyzed in a companion paper by *Graber et al.* [1996], and the reader is urged to read their paper in conjunction with the present one. Our first objective is to attempt to correlate the signatures appearing in the radar backscatter imagery with water mass structure and

current boundaries. Because a time sequence of images is available, additional inferences may be drawn about the translation and propagation of features. All this serves to build confidence in our ability to interpret features in the SAR images. In addition to the backscatter data, measurements were made in interferometric synthetic aperture radar (INSAR) mode. *Graber et al.* [1996] show how pixel-to-pixel phase differences in these INSAR data can be converted to radial surface currents. To make this conversion requires that the phase differences associated with the wind drift layer and with the motion of surface waves be carefully accounted for. This is because the phase difference, which is related to the mean Doppler frequency, can be biased through the same tilt modulation effects that influence the backscatter intensity [*Thompson*, 1989; *Thompson and Jensen*, 1993]. Thus spatially changing wave- and wind-induced surface motions may lead to spurious currents even when no ambient current field is present. Because of the importance of across-front surface current gradients (especially current convergence) in determining SAR signatures, a second objective of the present paper is to investigate whether the small-scale frontal changes inferred from the INSAR data are realistic when compared with the in situ current measurements.

The paper is arranged as follows. Section 2 discusses the instrumentation. Section 3 gives an overview of the hydrography and currents. Section 4 presents the SAR backscatter imagery. From these we identify signatures corresponding to water mass fronts and internal waves. Section 5 compares the across-front INSAR data with the in situ measurements of across-front current; also, the across-front radar modulation at the L band is compared with data acquired at longer and shorter radar wavelengths. Section 6 compares the observed frontal morphology and translation with earlier studies, and conjectures are made regarding a dark frontal signature and the origin and dissipation of the internal wave signatures.

2. Instrumentation

2.1. Airborne Measurements

The SAR data were collected on June 20, 1993, aboard the DC-8 AirSAR aircraft operated for NASA by the Jet Propulsion Laboratory. In this paper we show results from two INSAR passes, pass 180-1 and pass 90-1, and two standard mapping passes, pass 180-2 and pass 90-2 (see Table 1). The pass number gives both the aircraft heading (°T) and data collection mode (1 means INSAR was used and 2 means mapping). The aircraft flew at an altitude of 8.5 km and at a speed of 200 m s^{-1}. The horizontal resolution of the images shown in this paper is about 10 m. The INSAR passes were orthogonal and partly overlapped, and this allowed *Graber et al.* [1996] to derive an approximately synoptic vector map of the surface currents. Roughly 1 hour after the INSAR data were collected, the same sea surface areas were imaged in the mapping mode at the P, L, and C bands. These frequencies correspond to radar wavelengths λ_r of 60, 24, and 5 cm, respectively. The polarization for all three frequencies was vertical transmit and vertical receive (V-V). Images for all three bands for pass 90-2 appear in *Thompson et al.* [1994], but here we show only the L band image for consistency with the INSAR measurements, which also used L band (V-V). The wavelength λ_B of the Bragg resonant ocean waves is given by

$$\lambda_B = \lambda_r / 2 \sin \theta$$

Table 1. Synthetic Aperture Radar (SAR) Passes Used in This Paper

Pass	Time, UT	Mode	Heading, °T	Flight Line	Radar View Direction	Image Shown as
180-1	1424	INSAR	180	75°19.4′W	eastward	Figure 5
90-1	1456	INSAR	90	35°21.4′N	northward	Figure 6
180-2	1525	mapping	180	75°19.4′W	eastward	not shown
90-2	1602	mapping	90	35°21.4′N	northward	Figure 8

Pass numbers give the aircraft heading and sampling mode (1 means INSAR was used and 2 means mapping was used). All data are *L* band, vertical transmit, and vertical receive.

where θ is the radar incidence angle. The images cover an incidence angle range of 20°–60°; so for the L band, λ_B varies from 35 to 14 cm across the images. The corresponding range in Bragg wavenumber $k_B = 2\pi/\lambda_B$ is 0.18–0.45 cm^{-1}.

All the magnitude images have been "stretched" and normalized to remove trends in the range direction due to antenna pattern and incidence angle variation, so image brightness variations are only approximately proportional to (the square root of) the radar cross section. The INSAR magnitude images in this paper portray the magnitude of the complex signal and contain basically the same information as a standard strip map SAR image. The corresponding images of INSAR phase are shown in *Graber et al.* [1996]. Where we show cuts across the images, they are made from the original data. *Graber et al.* [1996] estimate the precision of the INSAR-derived currents as 2 cm s^{-1} for 10-m pixels and the accuracy as about 10 cm s^{-1} as determined from spatially averaged comparisons with other measurements.

2.2. Shipboard Measurements

Simultaneous with the airplane flights, in situ measurements were being made from the USNS *Bartlett*. Currents were measured with a 600-kHz broadband acoustic Doppler current profiler (ADCP). The ADCP, towed from the starboard side of the ship, was held outside the ship's wake by a kited surface float [*Marmorino and Trump*, 1996]. Current measurements, referenced to the bottom, were made every 2 s over 0.5-m-depth bins. Data were later averaged over 20 s. The shallowest measurement is centered at 1.7-m depth. From manufacturer's specifications the estimated accuracy of a single measurement (one depth bin, 20-s average) is about 4 cm s^{-1} (standard deviation); however, in practice, errors were closer to 10 cm s^{-1} because wave-induced platform accelerations degraded the measurement of attitude (pitch, roll, and heading).

Hydrographic measurements were made at 0.75-m depth with a conductivity-temperature-depth (CTD) probe attached beneath the ADCP and with a separate CTD towed astern of the ship and either winched vertically or held at a fixed depth of about 5 m (the ship's draft was 4.5 m). Some additional measurements were provided by investigators aboard the R/V *Columbus Iselin*. These included underway surface temperature readings and 1-m depth temperature and salinity measurements made from a towed catamaran.

SAR imagery was unavailable to the ship, so the sampling strategy was simply for the *Bartlett* to sail along a predetermined target latitude until there was clear reason to change direction or until the ship reached the outer detection limit of other sensor systems. The ship's navigational radar display, other real-time data displays, and visual sightings were all

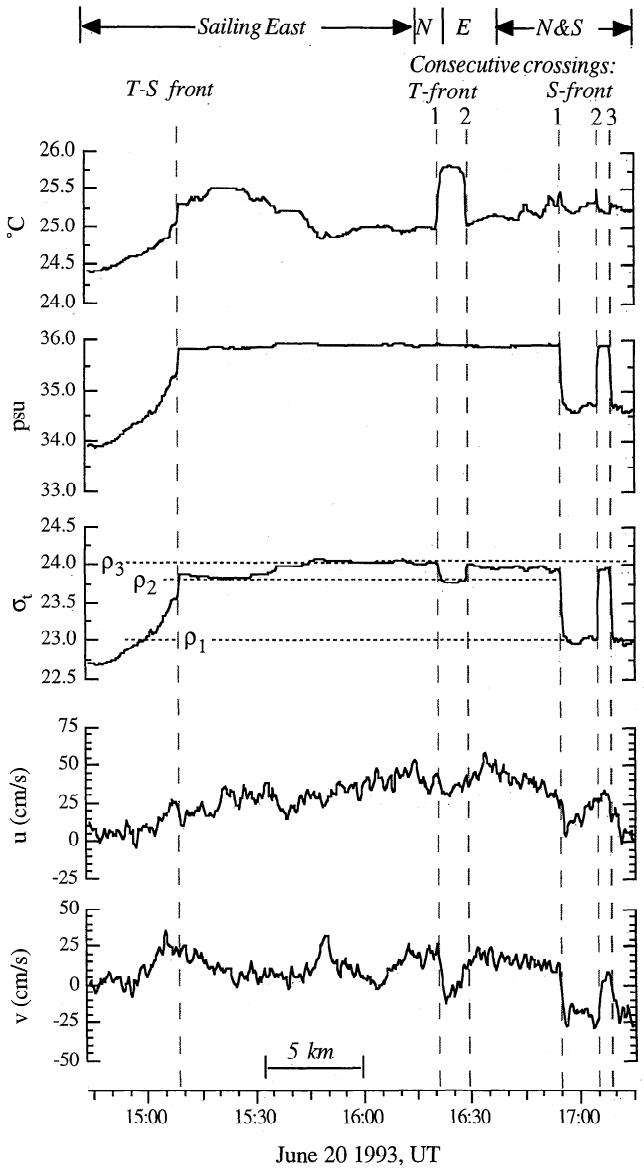

Figure 2. Time series of near-surface hydrography and currents from 1445 to 1715 UT. Data show eastward transect along 35.445°N, followed by two consecutive crossings of the temperature (T) front and three crossings of the salinity (S) front. Data are 20-s averages, and the ship's speed was about 3 m s^{-1}, so the horizontal resolution is about 60 m.

helpful in detecting the fronts and in indicating where frontal crossings should be made. In addition, video recordings of the sea surface were made, and these were examined for frontal signatures such as lines of weed, foam, and breaking waves.

2.3. Shore-Based Radar and Moorings

Additional instrument systems deployed during the 1993 High-Resolution field program included a shore-based Ocean Surface Current Radar (OSCR) and two moorings. OSCR was deployed from June 11 to July 8, 1993, by the University of Miami [*Shay et al.*, 1995] and consisted of two HF (25.4-MHz) radar transmit-receive seaside stations located in Avon (master station) and Waves (slave station), North Carolina (Figure 1). OSCR mapped the currents at 20-min intervals and 1.2-km horizontal resolution over a 30- by 45-km domain (Figure 1). Each measurement is an average over about 5 min in time and over the upper 0.4 m of the water column. The accuracy of the OSCR radial currents is 7–8 cm s^{-1}, but errors differ for east and north current components and vary systematically over the measurement domain [*Chapman et al.*, 1997].

Winds and directional wave spectra were measured at two discus buoys, DW and DE (Figure 1), both moored in about 30 m of water. Also, each mooring had a current meter and hydrographic sensors, at 13.8-m (DW) and 9.5-m (DE) depths [*Shay et al.*, 1995; *Chapman et al.*, 1997].

3. Experiment Setting

Measurements made from the *Bartlett* of near-surface hydrography and currents are shown in Figure 2. As indicated at the top of the figure, the ship's course over the period shown consisted of an eastward leg (along the target latitude of 35.445°N) followed by shorter north-south legs. Vertical dashed lines in the figure indicate crossings of three fronts: a "TS front," having changes in both temperature and salinity (but a density change dominated by salinity); a "T front," showing a change in surface temperature alone; and an "S front," where only salinity changes. These fronts separate water masses having three distinct density ranges, denoted in the figure by horizontal lines at density values $\rho_1 < \rho_2 < \rho_3$. By comparing the locations of the frontal crossings and the frontal orientations as inferred from the imagery presented in the next section we deduce that the freshest surface water (density ρ_1) occurs in the northern and western parts of the study area, the most dense water (ρ_3) occurs in the southeast, and water of intermediate density but highest temperature (ρ_2) occurs between the other two. Thus the surface density increases in the offshore (southeastward) direction. Across-front changes in the near-surface current (Figure 2) will be examined in section 5. Distinct color changes across the fronts were also observed visually at sea (not shown).

Hydrographic sections made along the target latitude are shown in Figure 3. The region in the upper left corner of the plot (just west of the T-S front) shows strong stratification (dominated by salinity changes) in the upper 10 m. Elsewhere, the water is weakly stratified with typical temperature and salinity values being about 25°C and 35.9 practical salinity units (psu). This is consistent with the moored measurements at midwater column depth (see below). These values indicate high-salinity water that originated from the Gulf Stream but has cooled while off the Georgia and South Carolina coasts [*Pietrafesa et al.*, 1985].

A water source southwest of Cape Hatteras is consistent with strong (≈50 cm s^{-1}) northeastward flow over the shelf measured on the previous day (June 19, not shown). Early on June 20, currents are still generally northeastward as shown by the OSCR current maps in Figure 4. The strongest flow (>1 m s^{-1}) occurs in the southeast part of the maps (nearest the Gulf Stream), and there is a broad current shear front (or, possibly, multiple smaller-scale shear fronts) extending northeastward from south of DW to north of DE; weaker flow occurs in the northeast part of the maps. Later in the day the entire flow field decelerates and rotates clockwise as the higher-speed fluid moves off the shelf.

During the joint ship and aircraft sampling the wind was 4–6 m s^{-1} from about 235°T as measured at the two buoys. Streaky structures ("wind rows") aligned approximately with the wind appear in the C band image for pass 90-2 shown by *Thompson*

et al. [1994]. A roughly 9-s period (80-m wavelength) swell was propagating from the southeast. The swell appears most clearly in the INSAR phase images in the paper by *Graber et al.* [1996].

4. SAR Imagery

In this section we discuss the four SAR passes: 180-1, 90-1, 180-2, and 90-2. Images for all but pass 180-2 are shown in Figures 5, 6, and 8, each reproduced to a common scale. The locations of passes 180-1 and 90-1 are indicated in Figure 1; the other two are nearly coincident with these. Overlain on each image is the track of the *Bartlett*. The radar reflection of the ship (labeled in each image) shows the ship's position at the image collection time. Each image is accompanied by an interpretive sketch highlighting features of interest and annotated with data from the ships and moorings. Narrow, shaded rectangles show locations of data cuts used to examine details of internal waves (this section) and fronts (section 5).

4.1. Pass 180-1 (1424 UT)

The dominant signature in Figure 5, collected at 1424 UT, is a bifurcated curve lying roughly in the north-northeastward direction. The *Bartlett* track crosses the SAR signature north of the bifurcation point at about the 1506 UT time mark whereas in situ measurements (Figure 2) show the ship crossing the T-S front at 1509 UT, about 1 km farther to the east. Thus, allowing for an eastward translation at about 35 cm s^{-1} from 1424 to 1509 UT, the SAR signature is the T-S front. This interpretation is also consistent with video recordings which showed a narrow (≈1-m-wide) line of foam coinciding with the T-S front, suggesting surface current convergence, and having a north-south orientation like that of the SAR signature near the ship's track.

South of the bifurcation point, an eastern branch of the SAR signature continues southward as a generally dark line. Measurements made across this branch by the *Columbus Iselin* (whose track is also shown in Figure 5) show no change in surface temperature but show that water on the east side has a high salinity of 35.9 psu, which is similar to the ρ_3-type water measured by the *Bartlett*. (Temperature and salinity values appear on the interpretative sketch in Figure 5.) The western branch of the SAR signature, which appears relatively bright in the image, trends to the southwest and may be extrapolated about 20 km to where, 3 hours earlier, the *Bartlett* zigzagged across another surface front oriented in a northeast direction (see the ship's track in Figure 1, 1208–1300 UT). Such an extrapolation roughly parallels the surface flow (compare Figure 4, current map at 1140 UT). At the earlier sampled front, near-surface measurements (see Figure 5, inset) show that water inshore has a low salinity (34.7 psu) similar to that of the ρ_1-type water, while the water lying offshore, i.e., in the wedge between the (extrapolated) western and eastern branches, has a higher but intermediate salinity (35.2 psu). Thus, in the area south of where the *Bartlett*'s track crosses the SAR line, there appears to be a confluence of (at least) three surface water masses, distinguished mostly by salinity differences and delineated by the branched SAR signatures. While surface salinity and density increase across these water masses toward the southeast, the locally deeper water has higher and more uniform salinity values (≈35.9 psu). This implies that the stratification ($d\rho/dz$) weakens southward of the *Bartlett*'s track, say, along 75.22°W.

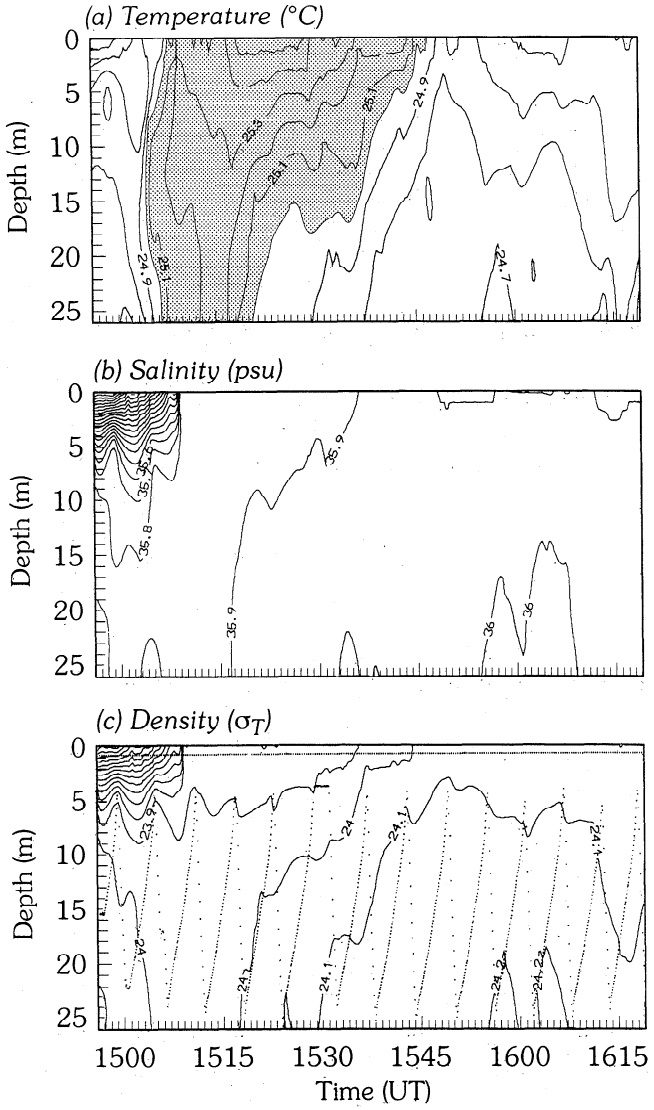

Figure 3. Hydrographic sections along 35.445°N: (a) temperature (>25°C, shaded), (b) salinity, and (c) density σ_T. Dots in the bottom panel show the location of the depth-oscillating towed CTD data (5-s averages) and 0.75-m depth conductivity-temperature-depth (CTD) data (20-s averages).

4.2. Pass 90-1 (1456 UT)

Figure 6 shows conditions about 33 min later and extending farther to the east. A northerly signature, which we will see below is the salinity front, extends eastward from the previous SAR curve and, in the eastern half of the image, assumes a sinuous form with a typical undulation having a radius of curvature of 2–3 km (see also below). A new, more southerly signature, which will be seen to correspond to the temperature front, occurs just north of the ship's track between 1545 and 1615 UT (75.04°–75.12°W). A close examination suggests this signature may bifurcate near the 1545 UT time mark: one branch crisscrossing the ship's track to the west and joining the T-S front; the other branch extending more to the southwest. We believe this structure accounts for the relatively warm water mass observed in the temperature section (Figure 3, shaded area) between the T-S front and the 1545 UT position.

In the western part of the SAR image, there are several groups (A–D) of east-west signals. As the hydrographic section

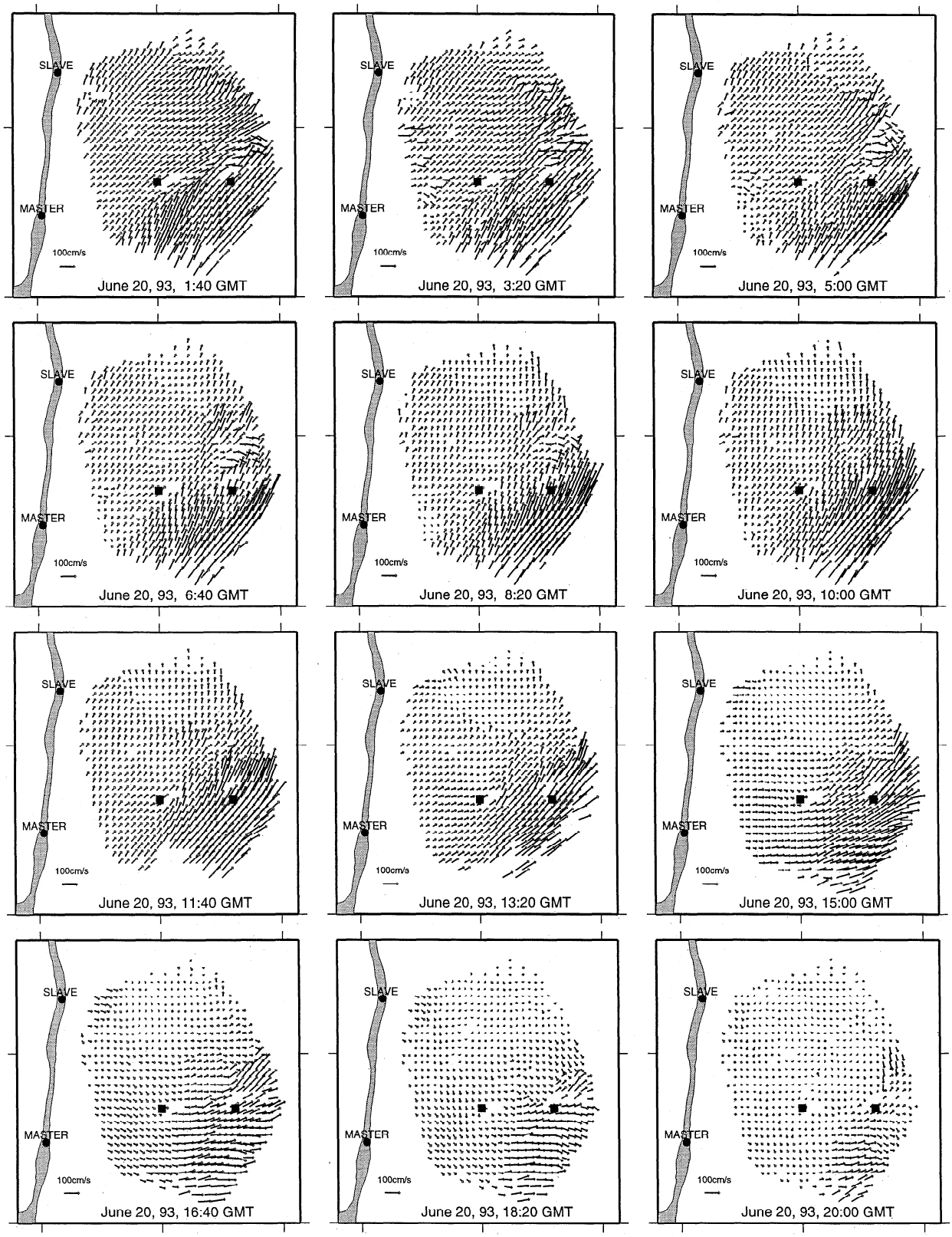

Figure 4. OSCR maps on June 20 shown at 100-min intervals. Solid squares show DW and DE moorings. Note deceleration and clockwise rotation of flow late in the day.

(Figure 3) shows strong, shallow stratification in the west, it is plausible to interpret these groups as packets of internal waves. While additional similar signatures appear north of the northerly SAR signature, no such signals occur in the weakly stratified water south of it. A cut through packet C (Figure 7) shows five waveforms. These have signal modulations $\delta\sigma/\sigma$ of about 10% relative to the background ($\sigma \approx 1$) and wavelengths increasing across the packet from about 90 m in the north to

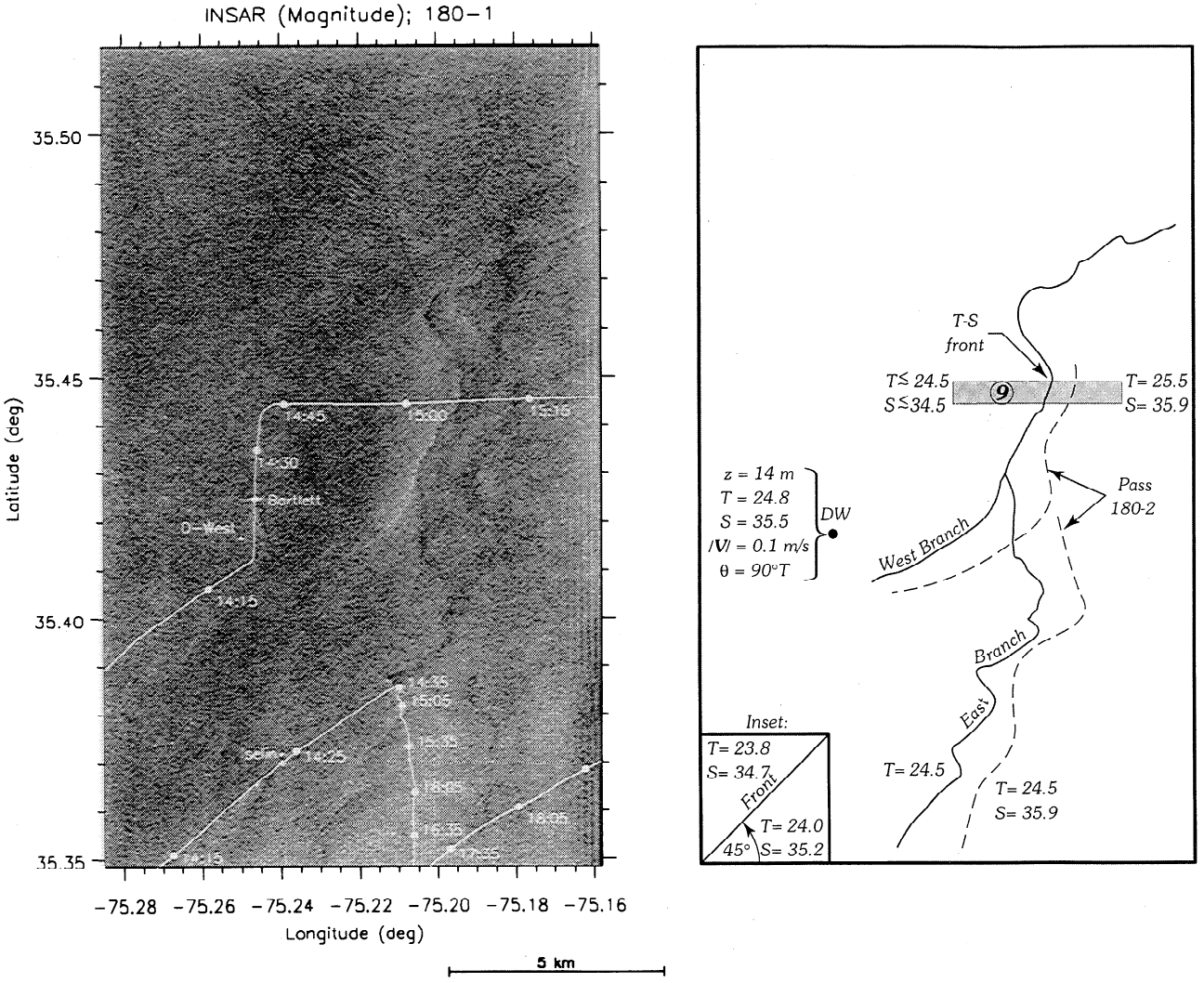

Figure 5. Pass 180-1 interferometric synthetic aperture radar (INSAR) magnitude image and interpretive sketch. Overlayed is the track of the USNS *Bartlett*, with dots marking successive 15-min positions; a separate dot highlights the reflection from the ship and indicates the ship's position at the time of the overpass. A second research ship (R/V *Columbus Iselin*) collected data in the southern part of the imaged area. Vertical stripes along the eastern edge of the image are a result of a large radar incidence angle and should be ignored. The sketch highlights the signatures of the temperature-salinity (T-S) front; annotations give near-surface temperature and salinity values as measured by the ships. Shaded strip in the sketch indicates data cuts used in later analysis (see Figure 9). Inset (lower left) shows property contrasts across a front lying 12 km southwest of the DW mooring and repeatedly crossed by the *Bartlett* from 1208 to 1300 UT (see Figure 1).

135 m in the south. As a soliton packet has longer waves at its leading edge and shorter waves at its trailing edge [e.g., *Apel*, 1995], we interpret the signals as solitons propagating southward (see below). Figure 7 also shows an identically positioned cut made through the pass 90-1 INSAR current image [*Graber et al.*, 1996, Plate 1]. The cut shows current fluctuations of several centimeters per second associated with the solitons. By chance the *Bartlett* apparently traversed the area between two packets, so no in situ current measurements are available for comparison. Figure 7 shows that maximum southward currents are offset southward from minima in the backscatter cut, and this, too, is consistent with southward propagation [e.g., *Gasparovic et al.*, 1988; *Thompson et al.*, 1988]. Some weak internal wave signals are visible only in the north part (upper left) of pass 180-1 where the angle between their propagation direction and the radar look direction is significantly less than 90°. The comparative lack of internal wave signatures in pass 180-1 is expected because the east-west propagating surface wave components to which the SAR is most sensitive are perpendicular to the internal wave-induced surface currents (for southward propagating waves), and according to wave-current interaction theory [e.g., *Gasparovic et al.*, 1988; *Thompson et al.*, 1988], their spectral modulation is small.

4.3. Pass 180-2 (1525 UT)

The image for this pass (not shown) shows only the signature of the north-south T-S front, and this is indicated by the dashed curves in Figure 5. It can be seen that the front, including the western and eastern branches, has moved roughly 1 km to the east from its position in pass 180-1 (made 1 hour earlier). This yields an eastward translation speed of about 30 cm s^{-1}. This

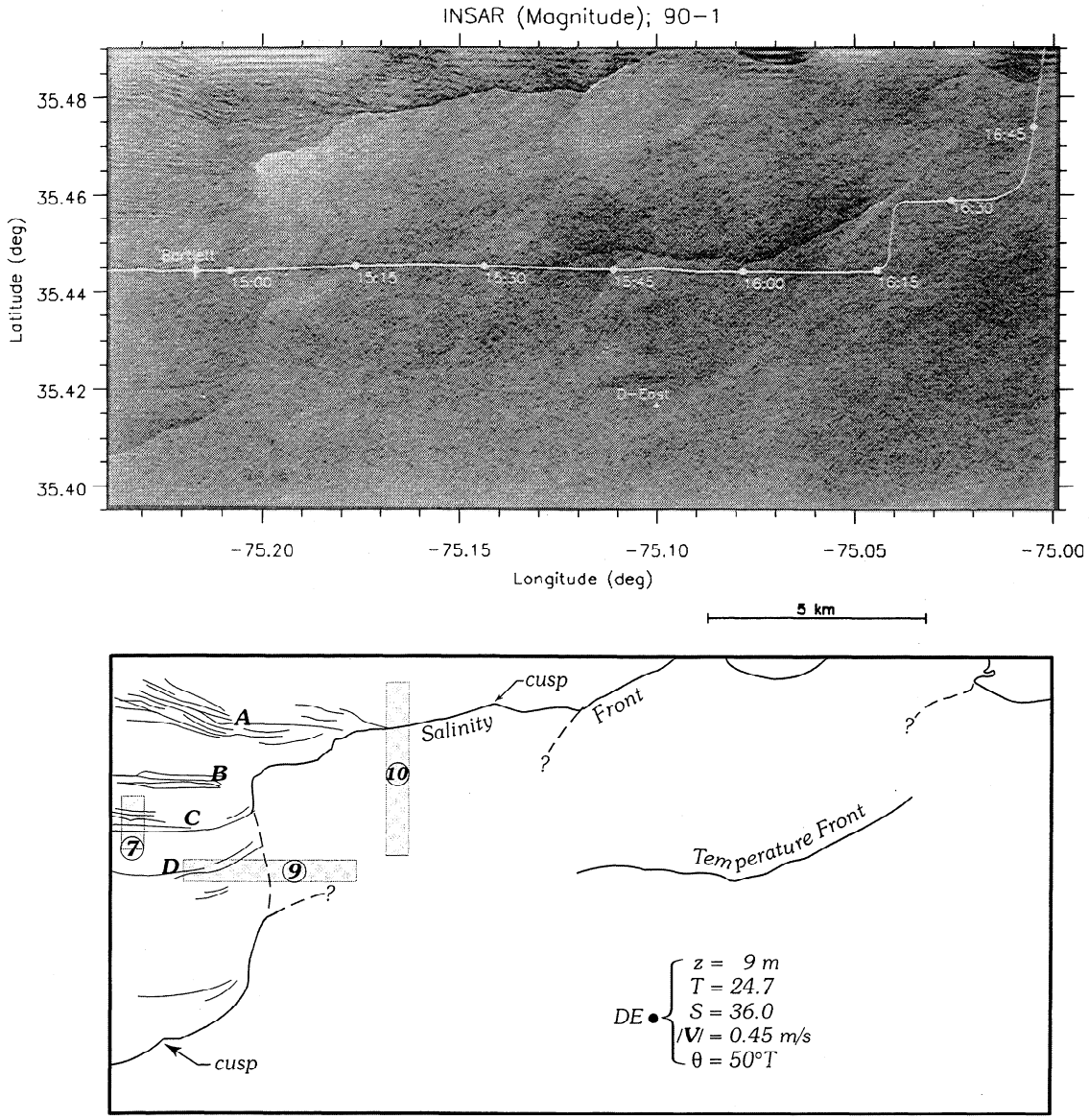

Figure 6. Pass 90-1 INSAR magnitude image and interpretive sketch. Data were collected about 33 min after those in Figure 5. Stripes extending across the top of the image are spurious. The sketch highlights the signatures of the S front and internal wave packets (A–D) occurring in the highly stratified water west of the S front. Shaded strips show data cuts used in later analysis (see Figures 9 and 10).

is comparable to the value found in section 4.1 and to the measured eastward current (Figure 2 and below).

4.4. Pass 90-2 (1602 UT)

Figure 8 shows nearly the same area as in Figure 6 but 66 min later. Except for the north-south T-S front all the same signatures still appear, but they are displaced somewhat from their previous positions (see below). In particular, the southerly SAR signature now intersects the ship's track in two places. This agrees with the ship's crossing of the T-front at 1621 and 1629 UT (Figure 2) where narrow (≈1-m-wide) weed lines were observed at sea which were oriented approximately northeastward like the SAR signature. Thus the southerly SAR curve is the signature of the T front. The northerly SAR line, still showing the large meanders noted earlier, crosses the ship's track at 35.49°N, about the same latitude at which the ship (53 min later) crossed the S front. Thus the northerly SAR line corresponds to the S front.

Frontal translation speeds can be derived by comparing the positions of the frontal signatures with the previous image. (The previous frontal positions are shown as dashed lines in Figure 8.) The T front is displaced eastward by about 1 km, which, dividing by the time between images, gives a translation speed of about 25 cm s^{-1}. The S front is displaced southeastward by about 500 m, so this gives eastward and southward translation speeds of about 10 cm s^{-1}. The eastward translation speeds are roughly comparable to ambient eastward currents of about 20 cm s^{-1}. (The ambient current is taken as the ADCP-measured mean over 10–20-m depth over the period between images.) However, southward translation of the S front is opposite the ambient northward mean current of about 15 cm s^{-1}. This result suggests the frontal signature is not

advected as a simple surface material line. We will return to this point in section 6.

A comparison of the soliton positions shows that if the four packets (A–D) in Figure 6 are translated together about 1 km directly southward, they overlay fairly well the ones in Figure 8. From this we infer a southward group velocity $c_g \approx$ (1 km)/(66 min) ≈ 25 cm s^{-1}. (We ignore the effect of the ambient current as it is generally eastward and perpendicular to the wave propagation.) Given the observed stratification, this value is comparable to a value of $c_g \approx 20$ cm s^{-1} calculated from the dispersion relation for first-mode internal waves of 100–200-m wavelengths. This supports interpreting the signals as freely propagating internal waves.

5. Frontal Signals

In this section, across-front cuts through the INSAR data (passes 180-1 and 90-1) are compared with the data from the *Bartlett*. (These cut positions are shown in the sketches of Figures 5 and 6.) We focus on the T-S and S fronts as their approximate north-south and east-west orientations allow the across-front convergence signal to be directly extracted from the INSAR data. As we have seen, the proximity of the INSAR and in situ data varies. For the T-S front the INSAR cut is made eastward along the ship's track, and there is up to a 54-min time offset between the measurements. For the S front, the time offset is nearly 2 hours, and because there is noise in the INSAR data near to where the ship crosses the front, the INSAR cut is made about 15 km to the west. We expect the local frontal dynamics to be relatively independent of changes in large-scale flow (see section 6.2), so across-front current gradients should still compare well even if small time and spatial offsets exist.

5.1. Across-Front Currents

Results for the T-S front are shown in Figure 9. Figures 9a–9c replot the shallow current data (averaged over 1.4- to 2.9-m depth) and near-surface density data from Figure 2 against across-front distance x. Also shown now is the deep current, taken as the mean over 10- to 20-m depth. The shallow current shows a broad zone of horizontal shear ($u_x > 0$ and $v_x > 0$) coincident with the gradual surface density increase west of the front and a change $\Delta u \approx -20$ cm s^{-1} at the sharp density front ($x = 0$). The convergence signal ($u_x < 0$) is confined to the shallow, low-density layer at the front; the deeper east current shows no change at $x = 0$. The INSAR east and north surface currents are compared with the shallow ADCP traces in Figures 9e and 9f. The comparison is fairly good near the front in the u component. The INSAR trace shows a change $\Delta u \approx 10$ cm s^{-1} across the front over a distance of about 50–200 m. Thus the across-front strain rate u_x is of the order of -1×10^{-3} s^{-1}, the negative sign indicating convergence. Away from the front, differences of the order of 10 cm s^{-1} occur between the INSAR and the shallow ADCP currents. While the inherent sampling errors are of this order (section 2), these systematic differences likely reflect a real vertical shear over the upper few meters of the water column of the order of 0.05 s^{-1} (i.e., 10 cm s^{-1} over 2 m). This is supported by the OSCR data (means and ranges in Figure 9f) which, overall, lie closer to the INSAR than the ADCP trace. [see also *Graber et al.*, 1997]. The vertical shear arises from the effects of wind drift, shallow stratification west of the front, and mean (positive) vertical shear due to the intruding, weakly stratified Gulf Stream flow to the east.

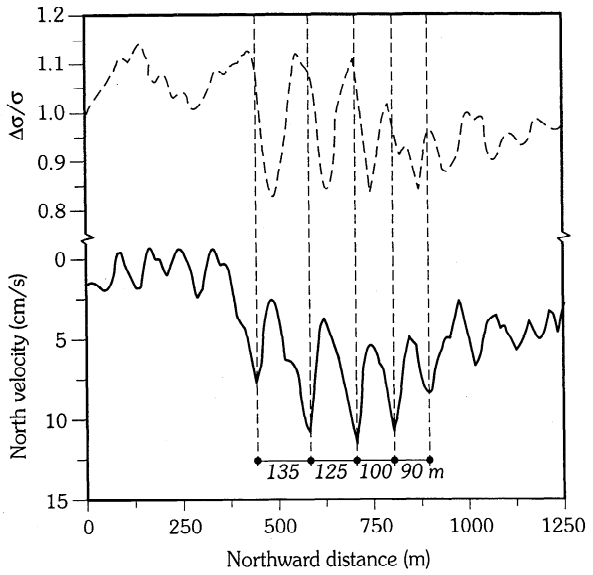

Figure 7. A northward cut through internal wave packet C. The top trace shows the radar backscatter signal from pass 90-1 (Figure 6); the bottom trace shows the north current derived from the corresponding INSAR phase data shown in *Graber et al.* [1996]. The occurrence of maximum southward currents (vertical lines) south of the backscatter troughs and the increasing wavelengths to the south suggest the signals represent a southward propagating soliton packet.

Current convergence occurs also at the east-west salinity front (Figure 10). The current change Δv is about -25 cm s^{-1} in the INSAR data and -30 to -40 cm s^{-1} in the shallow ADCP data. Again, there is no change in the deep ADCP data across the front, which is consistent with a shallow frontal layer. In this case the ADCP and INSAR traces have a substantial mean offset of about 25 cm s^{-1}. This results primarily from the 2-hour difference in sampling time in the presence of a decelerating and rotating background flow (Figure 4). This is supported by the observation that the OSCR data measured over that 2-hour period span the INSAR and ADCP curves (Figure 10d). Also, this could explain why the pass 90-1 currents north of the front are positive despite the southward translation of the front by the time of pass 90-2. The ship's two subsequent crossings of the S front also show across-front current changes of 15–20 cm s^{-1} (Figure 2, 1705 and 1709 UT). Also, a 30–50 cm s^{-1} change in the north current was measured by a shipboard X band Doppler radar while the *Bartlett* sailed north of and parallel to the S front, west of 75.005°W, from 1717 to 1720 UT (N. Allan, personal communication, 1995). The frontal width over which all these velocity changes occur is $\Delta y \approx 100$ m. Thus the across-front strain rate v_y is of the order of -5×10^{-3} s^{-1}. The across-front change in east velocity, measured only by the ADCP, is no more than about 20 cm s^{-1} (Figure 2), so the magnitude of the across-front shear u_y is estimated as, at most, 2×10^{-3} s^{-1}. Comparisons across the T front (not shown) also show good agreement between the northward INSAR and ADCP current components.

5.2. Across-front Radar Modulations

Radar intensity modulations across the T-S and S fronts are shown in Figures 9d and 10c. In each case the signal on the

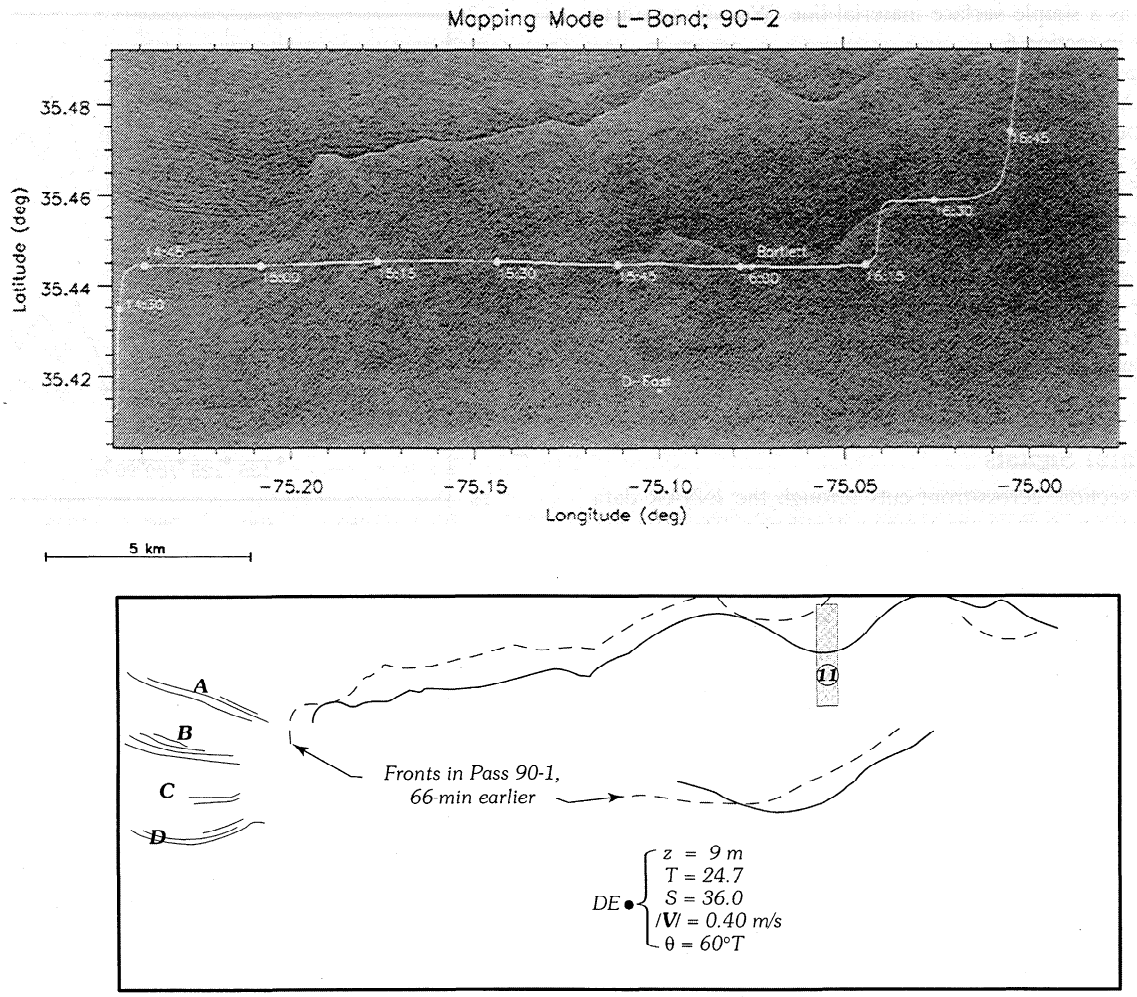

Figure 8. Pass 90-2 SAR image and interpretive sketch. Data were collected about 66 min after the image in Figure 6. S and T frontal signatures (solid lines) are displaced southward from their positions in the previous image (dashed lines). Likewise, internal wave packets (A–D) are displaced about 1-km southward from their previous positions. Shaded strip shows data cut used in later analysis (Figure 11).

upwind side of the front increases from an ambient level ($\Delta\sigma/\sigma \approx 1$) to a maximum at the upwind edge of the velocity frontal change. This is followed by an abrupt drop to the minimum level in each case. This bright-to-dark transition occurs over a length scale comparable to the width of the velocity front and is, in turn, followed by a recovery toward ambient downwind levels over a distance of 100–300 m. These transitions are of interest because they are not predicted by existing models (section 1).

The bright-to-dark transition is explored further for the case of the S front by making across-frontal cuts through the P, L, and C band data from pass 90-2 (Figure 11). These northward cuts are located along 75.055°W, where the front is locally east-west (see Figure 8 for cut location). Across-front cuts made at other positions yield similar results. The trace for each radar band has a peak near the front, but only the P and L band traces show a subsequent transition to a dark region or signal trough downwind of the front. The peaks in the P and L band traces are about 1.6 dB above ambient levels upwind of the front, while the peak in the C band trace is only about 0.4 dB. The peaks represent a combined increase in spectral density at the appropriate Bragg wavelength (42, 17, and 3.5 cm) and in tilt modulation as longer waves are refracted and shortened at the front. Finding signal levels of the order of 1 dB and the least modulation at the smallest radar wavelength is consistent with theoretical studies of the interaction of short surface and electromagnetic waves with convergent ocean fronts [e.g., *Lyzenga*, 1991]. Of more interest, however, is the behavior of the signal trough. At the P band the trough is about 1.2 dB below ambient downwind levels and is about 300-m wide. At the L band the trough represents a 0.9-dB depression and is about 150-m wide, which is comparable to the width measured from the L band INSAR magnitude cut in Figure 10. There is no clear trough in the C band trace. Thus, just like the radar peaks, the troughs become more pronounced with an increase in radar wavelength. A possible explanation for this is discussed in section 6.

6. Summary and Discussion

6.1. Summary

A case study has been made of coastal water mass fronts occurring off Cape Hatteras as revealed in high-resolution airborne SAR imagery and in simultaneous data from in situ sensors. The dataset is unique in having a time sequence of

imagery that includes INSAR current measurements. By correlating signatures in the imagery with hydrographic data we are able to describe the water mass structure over a broad area of the shelf. Fronts separating the different water masses appear as curvilinear SAR signatures 20 km or more in length, similar to those detected previously from space [*Fu and Holt*, 1982]. The length and position of the signatures agree qualitatively with currents measured by an OSCR system [see also *Graber et al.*, 1996].

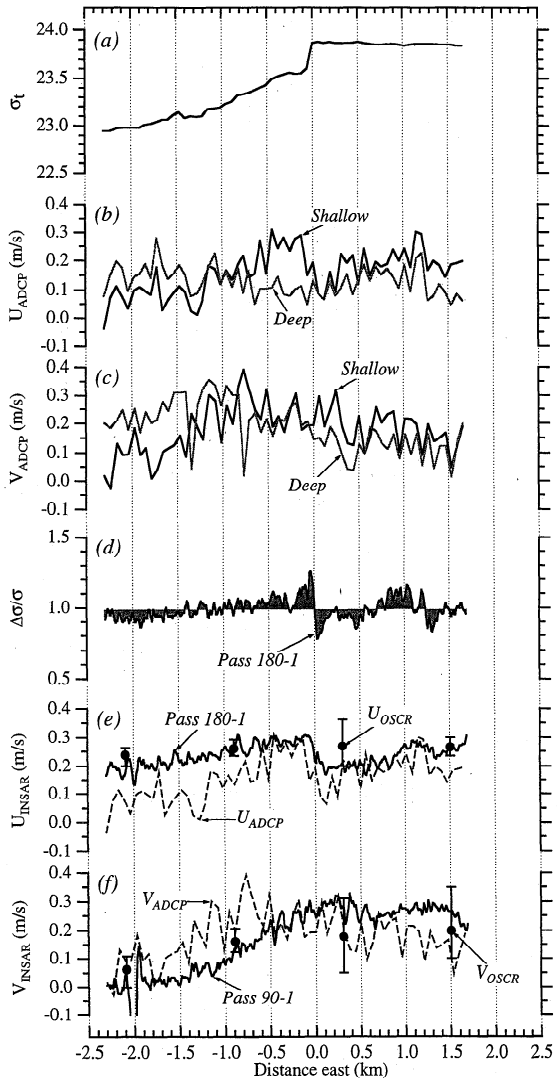

Figure 9. Eastward data cuts across the T-S front. (a) The σ_T at 0.75-m depth. (b) East ADCP currents from 1457 to 1518 UT averaged over 1.4–2.9-m depth (heavy curve) and 10–20-m depth (light curve). (c) North ADCP currents. (d) relative radar modulation for pass 180-1. The data cut is 500-m wide and parallel to the ship's track (see Figure 5.) Shading has been added to emphasize fluctuations about $\Delta\sigma/\sigma = 1$. (e) East INSAR current (solid curve) versus shallow ADCP current (dashed curve). Dots and vertical lines show mean and range of OSCR currents over the corresponding time period and along 35.444°N. Current convergence $u_x < 0$ occurs at $x \approx 0$ in both the INSAR and ADCP traces. (f) North INSAR current (solid curve) versus shallow ADCP current (dashed curve). INSAR values near $x = -2.0$ km are contaminated by reflection from research vessel. INSAR and ADCP currents show strong horizontal shear $v_x > 0$ over the broad region of surface density change ($x < 0$), little change across the convergent front ($x = 0$), and relatively weak horizontal shear to the east ($x > 0$).

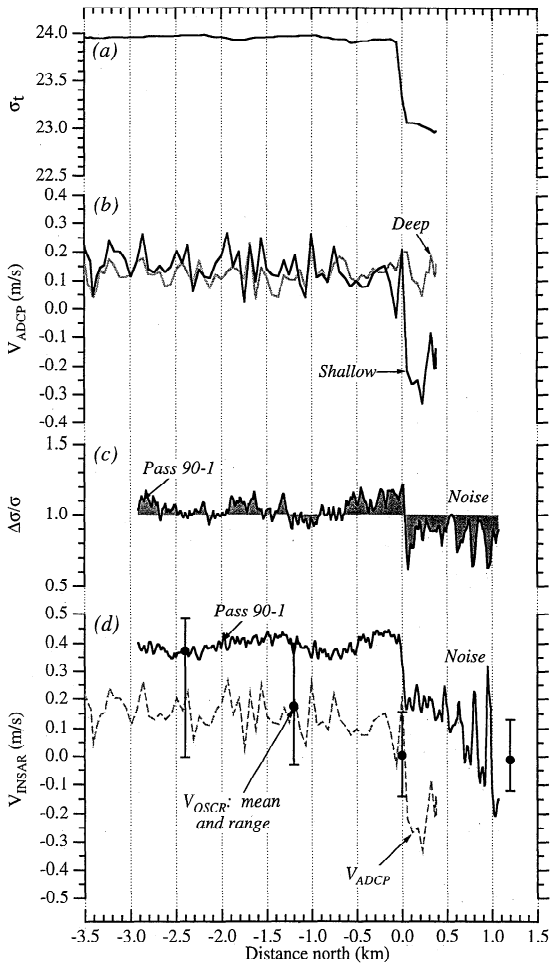

Figure 10. Northward data cuts across the S front. (a) σ_T. (b) North ADCP velocity from 1634 to 1659 UT. The shallow data show convergence $v_y < 0$ across the front ($y = 0$). (c) Relative radar modulation for pass 90-1. The data cut is 500-m wide and centered along −75.166°W (see Figure 6). These data are aligned (at $y = 0$) with in situ measurements made across the front about 15 km to the east. Large oscillations between 0.5 and 1.0 km distance are noise and correspond to the pattern of spurious east-west lines evident in the SAR image. (d) North INSAR current (solid curve) compared with shallow ADCP (dashed curve) and OSCR data. OSCR data are from −75.085°W (halfway between the SAR cut and the ship's track). ADCP and INSAR traces show similar frontal convergence signals. Mean levels differ in part because of time changes, as reflected in the large range of the OSCR data.

The fronts occurred during an incursion onto the shelf of relatively high-speed, dense water derived from the Gulf Stream. Rapid frontogenesis leading to convergent surface fronts is expected for this situation (see below). As similar episodes of alternating incursion and retreat recur at 3- to 5-day intervals, the data we show are likely typical of the incursion phase. While the present SAR data cover a relatively short period (about 2 hours), the fronts persist over the timescale of an episode as revealed in the OSCR maps. This suggests that a particular SAR signature might be observable for of the order of 10 hours. Thus SAR imagery over this area is

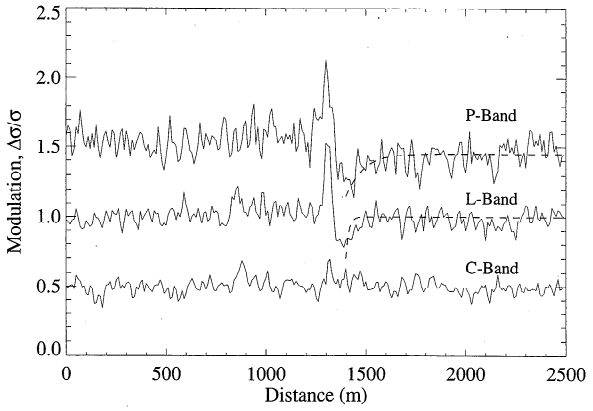

Figure 11. Northward cuts at the P, L, and C bands made across the S front in pass 90-2. The cut location is indicated in Figure 8. To reduce noise, the cut width is 500 m and data are smoothed in the cut direction using a 30-m running average. For clarity, traces for the P and C bands are offset by 0.5 units. Dashed curves show computed exponential growth of the P and L band Bragg components.

likely to be generally informative of fronts and water mass structure.

The time sequence of images allowed the evolution of particular fronts to be studied and inferences to be drawn about internal wave propagation. By focusing on the clearest frontal signals sampled jointly by the INSAR and the ship we were able to demonstrate that the INSAR measurements show changes in relative current (across-front convergence and shear) that are consistent with the in situ ADCP measurements. This supports *Graber et al.*'s [1996, Plate 4] high-resolution two-dimensional current map, which they synthesized from the two orthogonal INSAR flights (passes 180-1 and 90-1), as showing real variability of surface currents associated with the different water masses and not spurious patterns associated with spatial changes in the surface-wave spectrum, for example. Having such accurate measurements of the surface current gradients is important for understanding the modulation of surface waves near the front which ultimately determines the character of radar backscatter, an example being the bright-to-dark transition found across the salinity front. Below we put into a broader perspective several issues pertaining to the S front, the bright-to-dark radar modulation, and the internal waves.

6.2. Salinity Front

Several comparisons can be made between the present measurements and a similar S front sampled over a 7-hour period on September 17, 1991, but located in the same area as the present study [*Marmorino and Trump*, 1994]. Similar to the structure we observe (Figures 6 and 8), the 1991 salinity front had large-amplitude 2- to 5-km long meanders as well as smaller-scale corrugations [*Askari*, 1992]. The meanders have a length scale comparable to the internal Rossby radius of deformation which, for a two-layer system, is given by [e.g., *Gill*, 1982]

$$Ro_i = f^{-1}\{g(\Delta\rho/\rho)h(H-h)/H\}^{1/2}$$

For the S front in this paper the upper layer depth $h \approx 10$ m (Figure 3), the water depth $H \approx 30$ m (Figure 1), the relative density difference $\Delta\rho/\rho \approx 10^{-3}$ (Figure 2), and the Coriolis parameter $f \approx 7 \times 10^{-5}$ s^{-1}. Thus $Ro_i \approx 3.6$ km, which is similar to a value of 3.7 km calculated by Marmorino and Trump. Another morphological similarity is that both the 1991 and the present S fronts have northward pointing cusps. For example, compare the cusp on the S front in pass 90-1 (Figure 6) to one sampled repeatedly by *Marmorino and Trump* [1994, Figure 9]. Each cusp occludes an angle of about 140° and points toward the less dense surface water. Cusps are often found in river plume and estuarine fronts [e.g., *Largier*, 1992]. On these smaller scales a cusp is thought to represent a funneling of the ambient water as it plunges at the front, creating vorticity of opposite signs in the less dense surface water on either side of the cusp. A cusp on the west branch signature (Figure 6), which points toward the less dense water to the west, falls within the area of *Graber et al.*'s [1996] velocity map, so that it might be possible (with higher-resolution currents than they show) to find evidence of such small-scale vorticity patterns in the INSAR data.

Motivated by the 1991 observations, *Mied et al.* [1996] have modeled the evolution of intrusions of denser water from the Gulf Stream into less dense water overlying a flat (30-m-deep) continental shelf. Many different initial conditions were investigated. In most cases, frontogenesis occurred quickly as the result of baroclinic effects and the tilting of planetary vorticity by (as we observe) positive vertical shear in the along-shelf flow. The resulting front (or internal hydraulic jump) has strong surface convergence and propagates southward relative to any ambient flow at speeds of 12–37 cm s^{-1} [*Mied et al.*, 1996, Table 2]. Mied et al. fit their calculated speeds to within about 10% with the expression $c \approx (0.5)\,(gh\Delta\rho/\rho)^{1/2}$, where h is the equilibrium frontal interface depth (typically 10 m) and $\Delta\rho$ the maximum initial density contrast for a particular run. *Marmorino and Trump* [1994] found that the 1991 S front translated northward at about 35 cm s^{-1} in an ambient 60 cm s^{-1} northward current, which implies a relative southward propagation speed of about 25 cm s^{-1}. In our case the SAR images show the S front translating southward at about 10 cm s^{-1} in the face of an opposing northward ambient flow of about 15 cm s^{-1} (section 4.4), giving again a relative southward propagation speed of about 25 cm s^{-1}. While a speed of 25 cm s^{-1} is within the range explored by Mied et al., we calculate smaller values (11–16 cm s^{-1}) using their expression. Nevertheless, these comparisons are sufficient to suggest that the frontal displacements in the study area may be due in part to frontal propagation through the ambient fluid. If this is correct, then the displacements encode information about both the ambient current and stratification, and it may be a difficult practical matter to separate the two.

6.3. Dark Region Found Downwind of a Surface Convergence Zone

In the model of *Johannessen et al.* [1996] a front having, in general, both convergence and shear will appear as either relatively bright or dark but not both as we observed in section 5.2. We speculate that the dark region appearing downwind of the S front in the P and L band data reflects the dissipation of the corresponding radar Bragg waves through steepening and breaking at the front. The steepening is a result of the usual wave-current interaction included in the model of *Johannessen et al.* [1996] or *Thompson et al.* [1988], but the effect of wave breaking is not explicitly included in these models, and we speculate that the spectral density of waves steepened beyond the breaking limit will be reduced to nearly zero. These spec-

tral components will then be regenerated downwind of the breaking position over a distance that depends on the growth rate for the spectral component of interest. The width of the dark region in the radar data will then be proportional to this distance.

To investigate this effect further, we can estimate the regeneration distance for the appropriate Bragg waves at each of the three SAR frequencies. For waves with group velocity c_g the wind regeneration distance scale is given by $c_g T_w$, where T_w is the regeneration timescale [e.g., *Phillips*, 1977]. The reciprocal of T_w is the wave growth rate β, which is given by *Plant* [1982] by

$$\beta(k) = 1/T_w = 0.04[u_*/c_p(k)]^2 \omega(k) |\cos(\phi)|$$

where u_* is the friction velocity, k is the wavenumber, $\omega(k)$ is the radian frequency, $c_p(=\omega/k)$ is the phase speed, and ϕ is the angle between the air flow and radar range direction. Using this expression with $u_* = 15$ cm s^{-1} (corresponding to a 4-m s^{-1} wind speed at 4-m height) and $\phi = 55°$, we find that the regeneration distance scale $c_g T_w \approx 42.7$, 7.3, and 1.0 m for the P, L, and C band Bragg waves, respectively. These values decrease to 20.2, 3.4, and 0.5 m for $u_* = 22$ cm s^{-1} (corresponding to a 6-m s^{-1} wind speed). The dashed curves superimposed on the P and L band traces in Figure 11 show the computed growth of the P and L band Bragg waves using an e-folding distance equal to twice the $c_g T_w$ values for a 4-m s^{-1} wind. As pointed out by *Plant* [1982], large uncertainty exists in the values of β; this uncertainty is exacerbated by the exponential dependence in the regrowth curves shown in Figure 11, so an exact fit to the measurements is not expected. However, the curves qualitatively do reproduce the observed trend in width of the dark regions downwind of the S front. No growth rate curve is shown in Figure 11 for the C band since those Bragg waves regenerate so rapidly that the exponential curve would appear as a vertical line; higher-resolution radar data would be needed to resolve this regeneration region. We plan to explore further the modulation across the salinity front in a future modeling study that uses the two-dimensional current field measured by OSCR and INSAR, the observed frontal shape, and the measured winds and wave spectra.

6.4. Internal Waves

Signals interpreted as soliton packets were found only in the strongly stratified part of the study area. A southward propagation direction was determined from the displacement of packets between successive SAR images and from the change in wavelength and the relationship between backscatter and INSAR velocity across an individual packet. As the mean isobaths trend northeastward, the solitons thus locally have a component of propagation in the offshore direction, toward the shelf break. Usually, internal waves propagate away from the break, where they are generated by tidal forcing [e.g., *Apel*, 1995]. A possible explanation for the observed propagation direction is that the solitons are generated in the north but from a part of the shelf break that curves shoreward. Such a site occurs about 25 km northeast of the soliton observations, where the 50- and 100-m isobaths bend abruptly toward the northwest (Figure 1). (Refraction by mean current shear over the shelf may further steer the waves.) However, it is unclear how to reconcile the ~1-km spacing between packets with an expected value of about 11 km (i.e., $c_g \approx 25$ cm s^{-1} times the M_2 tidal period) for tidally generated wave packets.

Another point is that the internal wave signals were observed to fade toward the south in Figures 6 and 8. As the radar's view of the scene is northward, the radar-resonant ocean waves lengthen toward the south; hence we expect the internal waves to show an increase in modulation to the south, other things being the same (section 1). Thus the observed decreasing modulation to the south suggests the internal waves are dissipating, that the effect of the solitons on the surface waves is favoring the shorter Bragg waves, or that the stratification is weakening over their trajectory (reducing the surface velocity and strain rate). We suspect the latter as the in situ measurements show the stratification weakening in the southwest part of the study area (section 4.1), but the measurements are too limited to allow a detailed comparison.

7. Conclusions

The present study has served to further illustrate the potential for study of coastal circulation, hydrography, and dynamics using synthetic aperture radar imagery (SAR). While several questions remain, we believe the following conclusions can be drawn from this work:

1. Long, curvilinear signatures in radar intensity imagery of the shelf region near Cape Hatteras correspond to water mass frontal boundaries that are sharpened during incursions onto the shelf of denser water derived from the Gulf Stream.

2. The signature of a shallow S front shows a kilometer-long cusp structure, longer meanders (on the scale of the local Rossby radius of deformation), and relative southward propagation through the ambient water, all similar to a previous study of an S front found in the same area in 1991.

3. Across-front current gradients derived from the interferometric synthetic aperture radar (INSAR) data are in reasonable agreement with the near-surface measurements made with a towed acoustic Doppler current profiler. Across the S front the convergence rate is of the order of 5×10^{-3} s^{-1}.

4. The S front appears in imagery collected at the P and L bands as primarily a bright-to-dark transition but only as a bright line at the C band. The existence of a dark region downwind of the front is shown to be qualitatively consistent with the regrowth of radar-resonant Bragg waves presumed to be dissipated within the frontal region.

5. Closely spaced packets of solitons were found in the most strongly stratified inshore water mass. These internal waves had surface current speeds of about 5 cm s^{-1} (determined from the INSAR data) and propagated at about 25 cm s^{-1} toward the south (and thus had a locally offshore propagation component).

While we believe these results indicate promise, it is clear that additional study is needed before quantitative geophysical information can be routinely extracted from the kind of SAR imagery analyzed in this paper. For example, it should be possible to use the high-resolution two-dimensional surface current maps derived by *Graber et al.* [1996] to examine in some detail the interaction between the surface waves and current. This may lead to a better understanding of the radar intensity modulations we have concentrated on in this paper. When such effects are understood well enough, it may be possible to deduce information about bulk properties of the water column on the basis of the radar data and model calculations. We expect to examine this possibility in a future paper.

Acknowledgments. This work is a contribution to the High-Resolution Remote Sensing Program, which was sponsored by the

Office of Naval Research. Thompson and Graber were funded by ONR contracts N00014-95-1-0046 and N00014-91-J-1775. The airborne data collection was made possible through the combined efforts of colleagues at the National Aeronautics and Space Administration, the U.S. Army Corps of Engineers, and the Jet Propulsion Laboratory. At-sea measurements were made with help from D. Andrews and D. Greenewalt, now both retired from NRL. We thank R. Chapman (APL/JHU) and J. Edson (WHOI) for sharing their hydrographic data collected aboard the R/V *Columbus Iselin*. The OSCR data were collected by D. Ross and L. Shay (RSMAS). S. Nikolic (RSMAS) and T. Donato (NRL) helped make several of the figures. This paper is dedicated to the memory of Kim Saunders (1945–1996).

References

Apel, J. R., Linear and nonlinear internal waves in coastal and marginal seas, in *Oceanographic Applications of Remote Sensing*, edited by M. Ikeda and F. W. Dobson, pp. 57–78, CRC Press, Boca Raton, Fla., 1995.

Askari, F., A multitemporal analysis of radar imagery for study of submesoscale ocean features (abstract), Eos Trans. *AGU*, *73*(43), Fall Meet. Suppl., 247, 1992.

Beal, R. C., V. Kudryavtsev, D. R. Thompson, S. Grodsky, D. G. Tilley, V. Dulov and H. C. Graber, The influence of the marine atmospheric boundary layer on ERS 1 synthetic aperture radar imagery of the Gulf Stream, *J. Geophys. Res.*, *102*, 5799–5814, 1997.

Chapman, R. D., L. K. Shay, H. C. Graber, J. B. Edson, A. Karachintsev, C. L. Trump, and D. B. Ross, On the accuracy of HF radar current measurements: Intercomparisons with ship-based sensors, *J. Geophys. Res.*, in press, 1997.

Chemi, L., H. C. Graber, D. B. Ross, and L. K. Shay, Fields of ocean surface currents during HIRES-1, *Tech. Rep. 93-004*, 113 pp., Rosenstiel Sch. of Mar. and Atmos. Sci., Univ. of Miami, Miami, Fla., 1993.

Fu, L.-L., and B. Holt, SEASAT views oceans and sea ice with synthetic-aperture radar, *JPL Publ.*, *81-120*, 1–200.

Gasparovic, R. F., J. R. Apel, and E. S. Kasischke, An overview of the SAR internal wave signature experiment, *J. Geophys. Res.*, *93*, 12,304–12,316, 1988.

Gawarkiewicz, G., T. M. Church, G. W. Luther, T. G. Ferdelman, and M. Caruso, Large-scale penetration of Gulf Stream water onto the continental shelf north of Cape Hatteras, *Geophys. Res. Lett.*, *19*, 373–376, 1992.

Gill, A. E., *Atmosphere-Ocean Dynamics*, San Diego, Calif., Academic, 662 pp., 1982.

Glenn, S. M., and C. C. Ebbesmeyer, Observations of Gulf Stream frontal eddies in the vicinity of Cape Hatteras, *J. Geophys. Res.*, *99*, 5047–5055, 1994.

Graber, H. C., D. R. Thompson, and R. E. Carande, Ocean surface features and currents measured with synthetic aperture radar interferometry and HF radar, *J. Geophys. Res.*, *101*, 25,813–25,832, 1996.

Graber, H. C., B. K. Haus, R. D. Chapman, and L. K. Shay, HF radar comparisons with moored estimates of current speed and direction: Expected differences and implications, *J. Geophys. Res.*, in press, 1997.

Hayes, R. M., Detection of the Gulf Stream, in *Spaceborne Synthetic Aperture Radar for Oceanography*, edited by R. C. Beal, P. S. DeLeonibus, and I. Katz, pp. 146–160, *Johns Hopkins Oceanogr. Stud.*, 1981.

Herr, F., C. Luther, G. Marmorino, R. Mied, and D. Thompson, Ocean surface remote-sensing program planned, Eos *Trans. AGU*, *72*(19), 214, 1991.

Johannessen, J. A., L. P. Roed, and T. Wahl, Eddies detected in ERS-1 SAR images and simulated in a reduced gravity model, *Int. J. Remote Sens.*, *14*, 2203–2214, 1993.

Johannessen, J. A., R. A. Schuchman, G. Digranes, D. R. Lyzenga, C. Wackerman, O. M. Johannessen, and P. W. Vachon, Coastal ocean fronts and eddies imaged with ERS 1 synthetic aperture radar, *J. Geophys. Res.*, *101*, 6651–6668, 1996.

Largier, J. L., Tidal intrusion fronts, *Estuaries*, *15*, 16–39, 1992.

Lyzenga, D. R., Interaction of short surface and electromagnetic waves with ocean fronts, *J. Geophys. Res.*, *96*, 10,765–10,772, 1991.

Marmorino, G. O., and C. L. Trump, A salinity front and current rip near Cape Hatteras, North Carolina, *J. Geophys. Res.*, *99*, 7627–7638, 1994.

Marmorino, G. O., and C. L. Trump, Preliminary side-scan ADCP measurements across a ship's wake, *J. Atmos. Oceanic Technol.*, *13*, 507–513, 1996.

Marmorino, G. O., R. W. Jansen, G. R. Valenzuela, C. L. Trump, J. S. Lee, and J. A. C. Kaiser, Gulf Stream surface convergence imaged by synthetic aperture radar, *J. Geophys. Res.*, *99*, 18,315–18,328, 1994.

Mied, R. P., C. Y. Shen, T. E. Evans, and G. J. Lindemann, Frontogenesis with ageostrophic vertical shears and horizontal density gradients: Gulf Stream meanders onto the continental shelf, *J. Geophys. Res.*, *101*, 18,097–18,104, 1996.

Nilsson, C. S., and P. C. Tildesley, Imaging of oceanic features by ERS 1 synthetic aperture radar, *J. Geophys. Res.*, *100*, 953–967, 1995.

Phillips, O. M., *The Dynamics of the Upper Ocean*, 336 pp., Cambridge Univ. Press, New York, 1977.

Pietrafesa, L. J., G. S. Janowitz, and P. A. Wittman, Physical oceanographic processes in the Carolina Capes, in *Coastal and Estuarine Sci.*, vol. 2, *Oceanography of the Southeastern U.S. Continental Shelf*, edited by L. P. Atkinson, D. W. Menzel, and K. A. Bush, pp. 23–32, AGU, Washington, D. C., 1985.

Plant, W. J., Relationship between wind stress and wave height, *J. Geophys. Res.*, *87*, 1961–1967, 1982.

Porter, D. L., and D. R. Thompson, Estimation of thermocline depths from SAR imagery and a two-layer density model, paper presented at International Geoscience and Remote Sensing Symposium, Inst. of Electr. and Electron. Eng., Lincoln, Nebr., May 27–31, 1996.

Shay, L. K., H. C. Graber, D. B. Ross, and R. D. Chapman, Mesoscale ocean surface current structure detected by high-frequency radar, *J. Atmos. Oceanic Technol.*, *12*, 881–900, 1995.

Thompson, D. R., Doppler spectra from the ocean surface with a time-dependent composite model, in *Radar Scattering from Modulated Wind Waves*, edited by G. J. Komen and W. A. Oost, pp. 27–40, Kluwer Acad., Norwell, Mass., 1989.

Thompson, D. R. and J. R. Jensen, Synthetic aperture radar interferometry applied to ship-generated internal waves in the 1989 Loch Linnhe experiment, *J. Geophys. Res.*, *98*, 10,259–10,269, 1993.

Thompson, D. R., B. L. Gotwols, and R. E. Sterner II, A comparison of measured surface-wave spectral modulations with predictions from a wave-current interaction model, *J. Geophys. Res.*, *93*, 12,339–12,343, 1988.

Thompson, D. R., H. C. Graber, and R. E. Carande, Measurements of ocean currents with SAR interferometry and HF radar, paper presented at 1994 International Geoscience and Remote Sensing Symposium, Inst. of Electr. and Electron. Eng., Pasadena, Calif., August 8–12, 1994.

H. C. Graber, Rosenstiel School of Marine and Atmospheric Science, University of Miami, Miami, FL 33149-1098.

G. O. Marmorino and C. L. Trump, Naval Research Laboratory, Code 7250, Washington, DC 20375-5351. (e-mail: marmorino@nrl.navy.mil)

D. R. Thompson, Johns Hopkins University, Applied Physics Laboratory, Laurel, MD 20707.

(Received December 5, 1996; revised April 29, 1997; accepted May 15, 1997.)